Earth and Planetary Science Letters 602 (2023) 117940

Contents lists available at ScienceDirect

Earth and Planetary Science Letters

journal homepage: www.elsevier.com/locate/epsl

Ecosystem responses of two Permian biocrises modulated by CO_2 emission rates

Wen-qian Wang [a], Feifei Zhang [a,*], Shuang Zhang [b,*], Ying Cui [c,*], Quan-feng Zheng [d], Yi-chun Zhang [d], Dong-xun Yuan [e], Hua Zhang [d], Yi-gang Xu [f], Shu-zhong Shen [a,*]

[a] State Key Laboratory for Mineral Deposits Research, School of Earth Sciences and Engineering, and Frontiers Science Center for Critical Earth Material Cycling, Nanjing University, 163 Xianlin Avenue, Nanjing 210023, China
[b] Texas A&M University, Department of Oceanography, College Station, TX 77843, United States
[c] Department of Earth and Environmental Studies, Montclair State University, 1 Normal Ave., Montclair, NJ 07470, United States
[d] State Key Laboratory of Palaeobiology and Stratigraphy, Nanjing Institute of Geology and Palaeontology and Centre for Excellence in Life and Paleoenvironment, Chinese Academy of Sciences, 39 East Beijing Road, Nanjing 210008, China
[e] School of Resources and Geosciences, China University of Mining and Technology, 1 Daxue Road, Xuzhou 221116, China
[f] State Key Laboratory of Isotope Geochemistry and Center of Excellence in Deep Earth Science, Guangzhou Institute of Geochemistry, Chinese Academy of Sciences, Guangzhou 510640, China

ARTICLE INFO

Article history:
Received 2 May 2022
Received in revised form 6 October 2022
Accepted 28 November 2022
Available online 13 December 2022
Editor: B. Wing

Keywords:
Guadalupian-Lopingian biocrisis
end-Permian mass extinction
uranium isotopes
marine anoxia
carbon emission rate
hyperthermal events

ABSTRACT

Carbon dioxide (CO_2) emissions and associated climate change are thought to have caused a number of widespread marine anoxia and mass extinction events in the geologic past. However, how marine ecosystems respond to different CO_2 emission patterns remains an important unresolved question. The geologic records of the Permian Period, which witnessed two mass extinctions associated with volcanic eruption (thus CO_2 emissions) but with vastly different biological responses, provide a unique window to address this issue. Here, we present a long-term uranium isotope ($\delta^{238}U$) record using marine limestones covering the latest Early Permian through Middle to Late Permian. The $\delta^{238}U$ values show two episodes of low values in the middle Capitanian and late Changhsingian, indicating two periods of expansion of marine anoxia during the Permian Period. We use a uranium isotope mass balance model to quantify the anoxic seafloor areas, and we further use a carbon cycle model (LOSCAR, Long-term Ocean Sediment Carbon Reservoir) based on observed $\delta^{13}C$ of marine carbonates, sea surface temperature records, and ocean surface pH data to quantify the carbon emission rates across the two biocrises. The uranium isotope mass balance model reveals that the anoxic seafloor area is three times larger during the end-Permian mass extinction (EPME, covering ~35% of the seafloor areas) than that during the end-Guadalupian event (EGE, covering ~10% of the seafloor areas). The CO_2 emission rates across the two biocrises modeled from the LOSCAR model show that the carbon emission rate across the EPME was at least five times faster than that during the EGE, with the best-fit $\delta^{13}C$ values of the input sources ranging from −8 to −12‰, indicating a predominant volcanic CO_2 source during the EPME, and close to −25‰ during the EGE. Comparing model results and observed proxy data led to the suggestion that the more severe ecosystem responses during the EPME, including higher extinction rate and larger extent of seafloor anoxia, are closely linked to the faster carbon emission rates compared to the EGE.

1. Introduction

Hyperthermal events in the geological past hold essential lessons for improving our understanding of how key elements of the Earth's environmental and biotic systems are affected by rising greenhouse gas levels. The end-Permian mass extinction event (EPME; ~252 Ma) and the end-Guadalupian extinction event (EGE; ~259.5 Ma) are two hyperthermal events linked to profound volcanism and rising CO_2 levels (Burgess et al., 2017; Chen and Xu, 2021), which perturbed the global carbon cycle, leading to widespread expansion of marine anoxia (Bond et al., 2019; Lau et al., 2016; White et al., 2018; Zhang et al., 2018a,b). The two episodes of CO_2 emissions, however, are associated with vastly different ecosystem responses. The EPME was the largest extinction event in the Earth's history associated with the extinction of ~81%

* Corresponding authors.
E-mail addresses: fzhang@nju.edu.cn (F. Zhang), shuang-zhang@tamu.edu (S. Zhang), cuiy@montclair.edu (Y. Cui), szshen@nju.edu.cn (S.-z. Shen).

https://doi.org/10.1016/j.epsl.2022.117940
0012-821X/

of marine species (Fan et al., 2020) and ~89% of terrestrial species (Viglietti et al., 2021). In contrast, the biodiversity loss during the EGE is less severe, more protracted, and evident in a limited number of fossil groups (e.g., fusulines) according to the latest studies (Fan et al., 2020; Shi et al., 2021). Despite less severe biological responses, the EGE was associated with the largest sea-level fall (Haq and Schutter, 2008), the lowest $^{87}Sr/^{86}Sr$ ratios during the Paleozoic (Korte et al., 2006), and worldwide hiatus (Shen et al., 2019).

The triggers of these two extinction events have been attributed to two episodes of profound volcanic CO_2 emissions related to the Siberian Traps Large Igneous Provinces (LIPs) (Burgess et al., 2017; see also a recent study by Zhang et al. (2021) who suggests volcanism from around the Palaeo-, Meso- and Neo-Tethys oceans may have played a role) and the Emeishan LIPs (Bond et al., 2019; Chen and Xu, 2021), respectively. These two episodes of volcanic CO_2 emissions have perturbed global carbon and sulfur cycles, as evidenced by the large excursions in both $\delta^{13}C$ and $\delta^{34}S$ (e.g., Black et al., 2018; Shen et al., 2013; Yan et al., 2013). Despite a number of studies that have focused on the environmental and ecological changes across the EPME and the EGE, the driving mechanisms that led to their different biological responses are largely unexplored. This is, in part, because the majority of prior studies have focused on individual events, and a comprehensive comparison between the two events is largely lacking. In this study, we investigate the link between volcanic CO_2 emission rate and the severity of ecological and environmental deterioration across the EPME and the EGE by quantifying the timing, duration, and extent of marine redox chemistry changes and modeling the rate and size of CO_2 emissions.

The uranium isotopic composition of marine carbonates ($\delta^{238}U$) has been well-calibrated in modern settings and has been increasingly used as a proxy to place quantitative constraints on the extent of global marine redox chemistry changes across key evolutionary intervals in Earth's history (Clarkson et al., 2018; White et al., 2018; Lau et al., 2016; Zhang et al., 2018a, 2020a). This is because the redox transformation of U(VI) to U(IV), which is driven by marine redox chemistry changes, is associated with a large uranium isotopic fractionation (Andersen et al., 2017; Rolison et al., 2017). During this redox transformation, the reduced and sparsely soluble U(IV) is preferentially enriched in the heavier ^{238}U, which is driven by the nuclear volume effects (Bigeleisen, 1996). As a result, during periods of expanded marine anoxia, the enhanced reduction of U(VI) to U(IV) and the associated removal of ^{238}U from the seawater will shift the $\delta^{238}U$ of seawater towards lower values (Tissot and Dauphas, 2015; Zhang et al., 2020b). This phenomenon has been observed in the modern Black Sea and many anoxic marine basins (e.g., Rolison et al., 2017). Because of the much longer residence time of U in the ocean than the mixing time of the ocean, the $\delta^{238}U$ of the seawater is thought to be uniform as evidenced by the modern ocean, where $\delta^{238}U$ measurements from different ocean basins and across different water depths give nearly identical values (Chen et al., 2018; Holmden et al., 2015). Therefore, the $\delta^{238}U$ of carbonate collected from one location have the potential to record the global marine redox conditions. This notion has been supported by studies on the Permian-Triassic boundary (Brennecka et al., 2011; Lau et al., 2016; Zhang et al., 2018a,b) and the Ediacaran-Cambrian transition (Zhang et al., 2018c; Tostevin et al., 2019), where multiple sections from different ocean basins during the same time yielded nearly identical $\delta^{238}U$ trends.

In this study, we generated a long-term $\delta^{238}U$ record using an expanded and successive Middle-Late Permian (Guadalupian-Lopingian) limestone section from the Xikou section, Zhen'an County, Shaanxi Province, to examine the differences in the marine redox chemistry changes across the two Permian extinction intervals. We then use the Long-term Ocean-Atmosphere-Sediment CArbon cycle Reservoir (LOSCAR) model (Zeebe et al., 2009) to quantify the long- and short-term response of the Earth's surface system to CO_2 forcing. By linking the rate of CO_2 injection, changes in marine redox chemistry, and the magnitude of marine biodiversity loss, we attempt to foster our understanding of the linkages between CO_2 emission rates and the ecosystem responses to different CO_2 forcing.

2. Geological settings

The Xikou section (33.23° N, 109.38° E) was located in the north margin of the South China Block in the eastern Palaeotethys during the Permian (Fig. 1). The Permian sequences were divided into nine formations, named Sanlichong, Shimenya, Yazi, Wulipo, Shuixiakou, Xikou, Yundoutan, and Longdongchuan formations in ascending order (Ding et al., 1989). Thick-bedded limestones were developed from the Sanlichong to the Wulipo formations, and the first occurrences of *Brevaxina*, *Neoschwagerina*, and *Presumatrina* were defined as the base of the Kungurian, the Roadian, and the Wordian stages, respectively (Wang et al., 2021). The Shuixiakou Formation contains middle- to thick-bedded limestone interbedded with siltstones and belongs to the Capitanian according to the occurrence of *Chenella* (Cheng et al., 2019; Wang et al., 2021). The GLB is characterized by an abrupt lithofacies transition from shallow-marine bioclastic limestone to coastal coarse-grained siliciclastic sandstone, corresponding to a rapid regression in South China caused by regional uplift associated with the eruption of the Emeishan LIPs. The Xikou Formation is composed of sandstone interbedded with limestone and siltstone. The occurrences of *Kahlerina*, *Codonofusiella*, and *Reichelina* suggest that the Xikou Formation can be ascribed to the Wuchiapingian stage. The Yundoutan Formation is characterized by thick to massive bedded reddish limestones with abundant brachiopods, corals, crinoids, and sponges. The Longdongchuan Formation contains thick to massive bedded white limestones. The first occurrence of *Clarkina wangi* was defined as the base of the Changhsingian stage. The Permian-Triassic boundary was defined by the first occurrence of *Hindeodus parvus*, in a 3.7 m-thick tuffaceous oolitic grainstone (Wang et al., 2021), which was capped by a volcanic ash bed.

A total of 85 micritic limestones were selected for $\delta^{238}U$ analyses. Those samples cover the Kungurian through the Induan stages. The age of individual sample was calculated by linear interpolation between age tie-points using the time scale of Shen et al. (2019), with some modifications from Wu et al. (2020) (Table 1).

Table 1
Time scale used in this study, the main scheme is after Shen et al. (2019), with some modifications after Wu et al. (2020).

Series	Stages	Age of the base (Ma)
Triassic	Induan	251.902±0.024
Lopingian	Changhsingian	254.14±0.07
	Wuchiapingian	259.51±0.21
Guadalupian	Capitanian	264.28±0.16
	Wordian	266.9±0.4
	Roadian	272.95±0.11
Cisuralian	Kungurian	283.5±0.6
	Artinskian	290.1±0.26
	Sakmarian	293.52±0.17
	Asselian	298.92±0.19

Fig. 1. Paleogeography of the Changhsingian with the base map provided by Scotese (2021), showing the position of the studied section.

3. Methods

3.1. Major and trace elemental analyses

About 1 gram of powder was dissolved in 45 mL 0.5 M HCl for 4-6 hours at room temperature. The supernatants were separated and dried on the hot plate and re-dissolved with concentrated HNO_3 three times to remove any HCl, after which the sample was dissolved in 3 M HNO_3. An aliquot of the stock solution was taken out and diluted to an estimated Ca concentration of 150 ppm. The 1 ppb element spikes of In, Sc, Y, and Bi were added for mass calibration. The elemental concentration was measured on a Thermo Scientific Finnigan Element 2 ICP-MS at the Yale Metal Geochemistry Center (YMGC). The precision of the analysis for the elements is better than 5% based on the long-term reproducibility of internal standards.

3.2. Uranium isotopes analyses

An estimated amount of supernatant corresponding to 250 ng U was taken out from the stock solution and dried down and re-dissolved in 3 mL 3 M HNO_3. The uranium was extracted from the solution after adding ^{233}U-^{236}U double spikes using UTEVA resin following the method of Zhang et al. (2018a,b). Each sample was put through the UTEVA resin twice in order to remove the matrix ions completely. The final purified U was dissolved in 2% HNO_3 and diluted to a U concentration of 50 ppb. The $\delta^{238}U$ was measured by Thermo Fisher Scientific Neptune plus MC-ICP-MC at YMGC. Samples were analyzed through the sample-standard bracketing method using the reference material of CRM-145a (U concentration of 50 ppb), and two laboratory standards, Ricca and CRM-129a, were also measured every fifteen samples. Sample $\delta^{238}U$ values were normalized by the average of the bracketing standards. The reproducibility of replicate measurements of $\delta^{238}U$ for CRM-145a was 0.07‰ (2SD, N = 134). Two laboratory standards, Ricca and CRM 129a yield $\delta^{238}U$ values of -0.20 ± 0.06‰ (2SD, N = 22) and -1.69 ± 0.07‰ (2SD, N = 22), respectively, which are in good agreement with published data (Chen et al., 2018; Zhang et al., 2018a,b, 2020b).

4. Results

4.1. Elemental concentrations

The stratigraphical distribution of U concentration was shown in Fig. 2, the elemental concentration of Mo, Fe, Mn, Sr, Al, and Rb were summarized in Fig. 3, and the detailed elemental concentrations were provided in Appendix 1. The U concentration of the samples ranges from 0.1 to 7.2 ppm (Fig. 2), and most of the samples (75%) contain U < 2 ppm. The Mo concentration varies between 1 ppb and 460 ppb with an average of 55 ± 71 ppb (1SD, N = 81; Fig. 3). The Fe concentration of the samples ranges from 13 ppm to 11289 ppm, with an average of 627 ± 1618 ppm (1SD, N = 81). The average Mn, Sr, Al, and Rb concentrations are 186 ± 194 ppm (1SD, N = 81), 647 ± 642 ppm (1SD, N = 81), 125 ± 155 ppm (1SD, N = 81), and 0.2 ± 0.2 ppm (1SD, N = 81), respectively.

4.2. The $\delta^{238}U$ of carbonates

The $\delta^{238}U$ values from our study vary between −0.79‰ and 0.11‰, with an average value of -0.25 ± 0.18‰ (N = 85, 1SD; Fig. 2). The $\delta^{238}U$ values stay relatively constant from the fusulinid *Misellina minor* Zone (about 0.4 km in the lithologic column in Fig. 2; correlates to the late Kungurian) to the *Neoschwagerina craticulifera-Verbeekina verbeeki* Zone (about 0.8 km in the lithologic column in Fig. 2; correlates to the Wordian). There are two negative shifts in $\delta^{238}U$ values in the stratigraphic records, which are within the fusulinid *Chenella changanchiaoensis* and *Colania douville - Kahlerina pachytheca* zones (about 0.9 km to 1.2 km in the lithologic column in Fig. 2; correlates to the early to middle Capitanian, prior to the EGE), in the Shuixiakou Formation, and the conodont *Clarkina changxingensis* Zone (about 3.1 km to 3.3 km in the lithologic column in Fig. 2; correlates to late Changhsingian, before the PTB), in the Longdongchuan Formation, respectively.

5. Discussions

5.1. Fidelity of the $\delta^{238}U$ data in recording the Middle-Late Permian Ocean redox chemistry

Diagenetic processes may alter the original chemical signals of carbonates. In the past several decades, several diagenetic indicators have been developed and applied to evaluate the overall preservation of carbonate rocks (Brand and Veizer, 1980; Gilleaudeau et al., 2019). In this study, we use those conventional geochemical indicators to test if the $\delta^{238}U$ values of the samples analyzed in this study record any non-marine signals.

5.1.1. Evaluation of the detrital contamination

The input of detrital U may influence the $\delta^{238}U$ values. It can be evaluated by Al concentrations and U/Al and Rb/Sr ratios (Zhang et al., 2018b, 2020b). Generally, the Al concentrations of the studied samples are low and do not co-vary with the $\delta^{238}U$ values ($r = -0.18$, $p > 0.05$). Most of our samples (74%, N = 60) yield U/Al ratios significantly higher than the upper continental crust ratio of ~0.331 ppm/wt.% (Rudnick and Gao, 2014). Furthermore, there are no apparent correlations between $\delta^{238}U$ values and U/Al (Table 2),

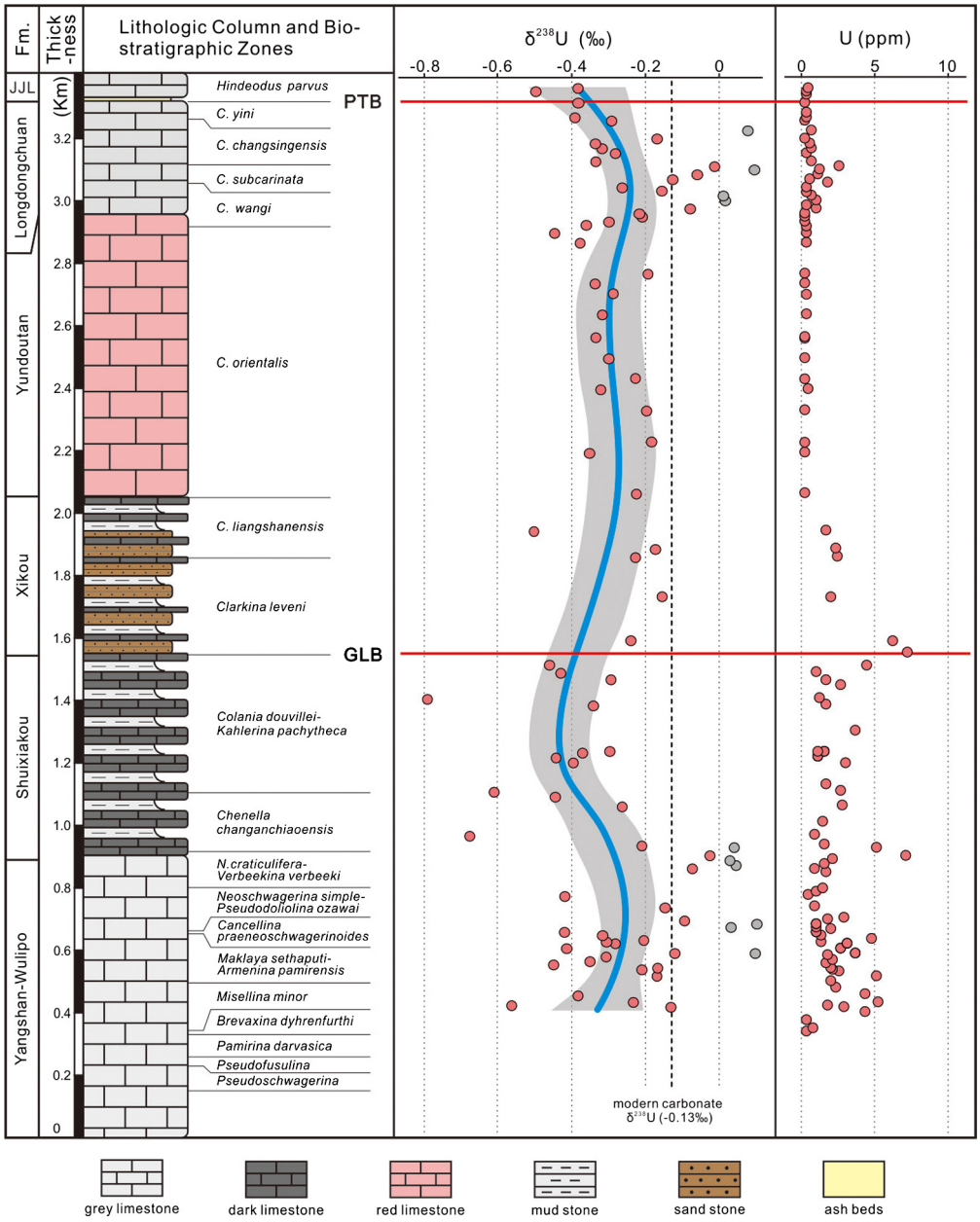

Fig. 2. The lithologic column, biostratigraphic zones, δ^{238}U results, and U concentration of the studied section. The red points represent samples that pass the diagenetic screening, and the gray points represent samples that may be diagenetically altered. (For interpretation of the colors in the figure(s), the reader is referred to the web version of this article.)

indicating that the observed δ^{238}U trends are unlikely related to detrital U inputs. In addition, all the samples have Rb/Sr ratios less than 0.01 (Fig. 4) and do not show any correlation with the δ^{238}U values ($r = 0.08$; $p > 0.05$), indicating that the digestion protocol did not involve U related to clay minerals.

5.1.2. Evaluation of meteoric diagenetic alteration

Meteoric diagenesis tends to increase Mn and Fe, and decrease Sr concentration of carbonates (Brand and Veizer, 1980). However, prior studies have used various thresholds of these proxies to screen for diagenesis (Derry et al., 1992; Kaufman and Knoll, 1995; Lau et al., 2016; Zhang et al., 2018b; Wang et al., 2022). For example, samples with Fe $<$ 1000 ppm and Fe $<$ 3000 ppm are both used in previous studies (Denison et al., 1994; Derry et al., 1992), and Mn/Sr ratios ranging from 1 to 10 are used in different studies (Kaufman and Knoll, 1995; Lau et al., 2016; Zhang et al., 2018b). The samples in this study generally contain low Fe concentrations (Fig. 3), with 89% of samples containing Fe $<$ 1000 ppm and 95% of samples $<$ 3000 ppm (Denison et al., 1994). However, we observed that those samples with higher Fe concentrations ($>$ 3000 ppm) have similar δ^{238}U values as those with lower Fe contents (Fig. 3). All the measured samples contain Mn/Sr ratios of less than 10 (Fig. 4), and 88% of the samples yield Mn/Sr ratios $<$ 1. Considering Fe and Mn concentrations depend on the redox chemistry of the sedimentary environment; we, therefore, checked the covariation between the δ^{238}U values and these diagenetic indicators to investigate if the samples are influenced by meteoric diagenesis. Cross correlation analysis shows that there are no apparent correlations between δ^{238}U values and Mn, Sr, Fe, concentrations and Mn/Sr ratios (Fig. 4; $|r| < 0.3$ for all proxies; $p > 0.05$ for Mn and Mn/Sr, $p < 0.01$ for Sr and Fe), confirming overall good preservation of the samples analyzed in this study.

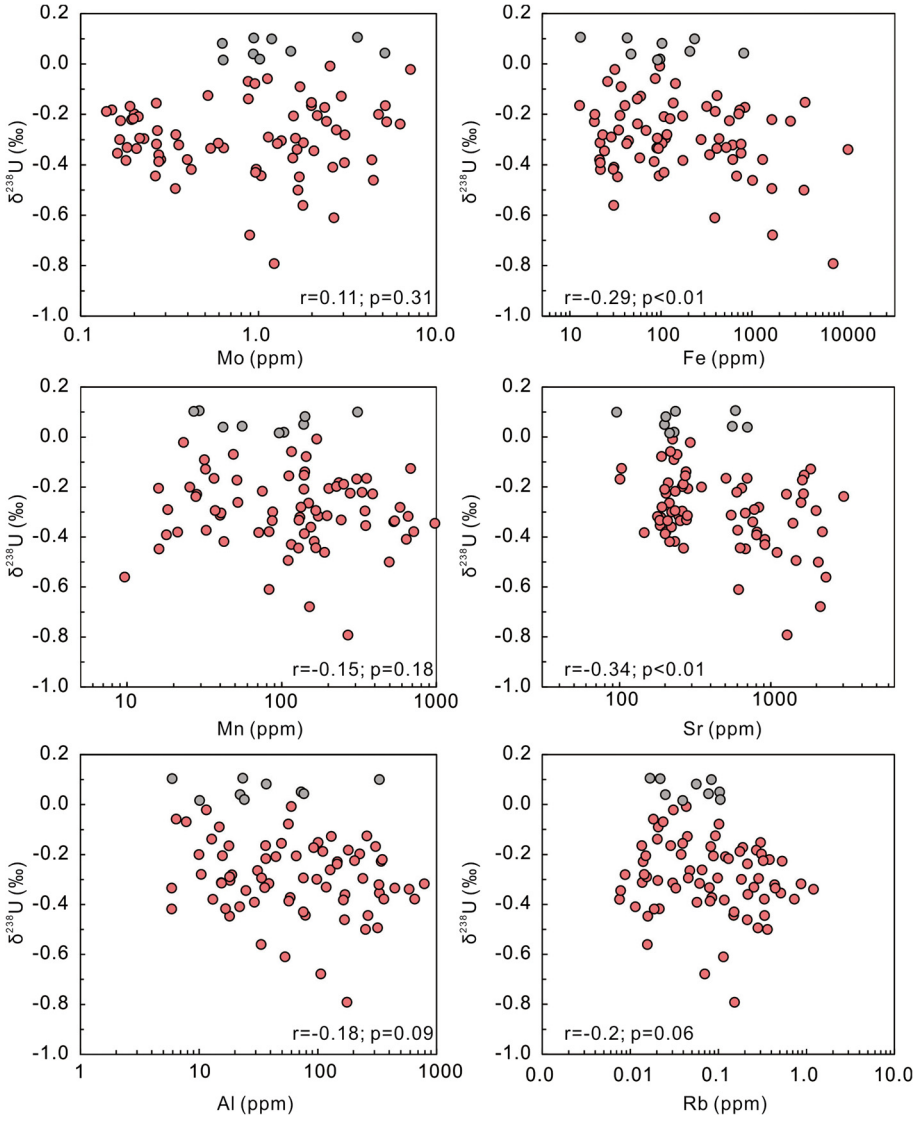

Fig. 3. Cross-plots between δ^{238}U and Mo, Fe, Mn, Sr, Al, and Rb concentrations, showing no co-variation between these proxies.

5.1.3. Evaluation of the influence of dolomitization on the δ^{238}U values

Dolomitization can occur through multiple different processes and may impact the original δ^{238}U signals, depending on the style and timing of this process (Gilleaudeau et al., 2019). We used Sr concentration, Sr/Ca ratio, and Mg/Ca molar ratio to evaluate the influence of dolomitization on δ^{238}U values (Figs. 3, 4). The δ^{238}U values of our samples show weak correlation with Sr concentrations ($r = -0.34$; $p < 0.01$) and Sr/Ca ratios ($r = -0.36$; $p < 0.01$), and no correlation with Mg/Ca ratios ($r < 0.1$; $p > 0.05$; Table 2), indicating negligible influence of dolomitization on the δ^{238}U values.

5.1.4. Evaluation of local pore water redox chemistry

Reducing porewater conditions associated with the degradation of organic matter within marine sediments will induce U isotope fractionation during the reduction of U(VI) to U(IV) (Andersen et al., 2017). We evaluate this process using U and Mo contents. The U contents do not co-vary with δ^{238}U values as seen in Fig. 2. In addition, the Pearson correlation statistical analysis between δ^{238}U values and U and Mo contents shows that there are no significant correlations between them ($r < 0.2$, $p > 0.05$ for U; $r < 0.2$, $p > 0.05$ for Mo; Table 2), indicating that the δ^{238}U values are not significantly affected by local pore water redox chemistry.

Table 2
Statistical analysis testing the diagenetic influence on the δ^{238}U record. We provided the Pearson Correlation Coefficient r value and related significance level (p value), all the r values between δ^{238}U and diagenetic proxies are less than 0.4, suggesting only weak or no covariation between these proxies.

Xikou section	Pearson test (r value)	Significance level (p value)
δ^{238}U vs. U content	0.14	0.20
δ^{238}U vs. Mn/Sr	0.11	0.31
δ^{238}U vs. Mn content	−0.15	0.18
δ^{238}U vs. Sr content	−0.34	0.002
δ^{238}U vs. U/Al	0.21	0.06
δ^{238}U vs. Th content	−0.18	0.11
δ^{238}U vs. Al content	−0.18	0.09
δ^{238}U vs. Mo content	−0.17	0.12
δ^{238}U vs. Fe content	−0.29	0.008
δ^{238}U vs. Rb/Sr	−0.07	0.50
δ^{238}U vs Mg/Ca	0.19	0.43
δ^{238}U vs Sr/Ca	−0.36	<0.01
δ^{238}U vs Rb	−0.20	0.06

Finally, the riverine U accounts for > 90% of U inputs to the oceans, with an average δ^{238}U value of −0.26‰ (Andersen et al., 2017; Tissot and Dauphas, 2015). Considering the fact that the major marine U sinks (i.e., anoxic and suboxic sedimentary sinks)

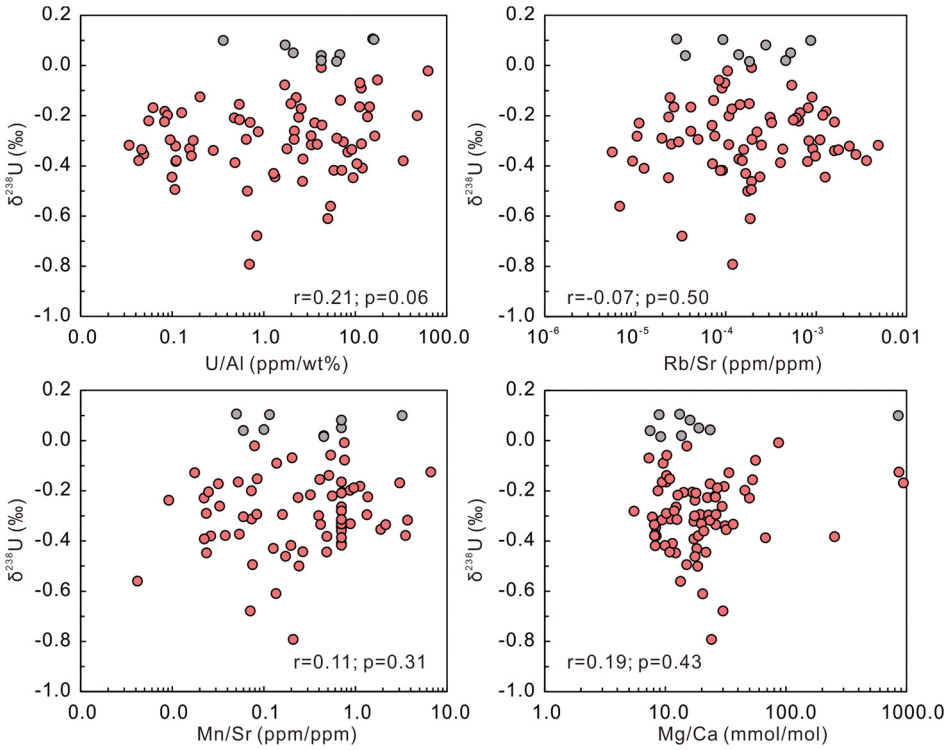

Fig. 4. Cross-plots between δ^{238}U and U/Al, Rb/Sr, Mn/Sr, and Mg/Ca ratios, showing no co-variation between these proxies.

Table 3
2σ uncertainty used in the uranium isotope mass balance model.

Parameter	Median	2σ	Reference
$\delta^{238}U_{sw}$ loess fit	−0.54‰	0.06 to 0.13‰	This study
Offset between δ^{238}U of calcite and the ocean	0.26‰	0.1‰	Romaniello et al., 2013; Chen et al. (2018)
$\delta^{238}U_{river}$	−0.3‰	0.04‰	Zhang et al. (2020b)
$N_{sw,0}$	9.36×10^{12} mol	0	Zhang et al. (2020b)
Uranium flux from river inputs (J_{river})	4×10^{7} mol yr^{-1}	0	Zhang et al. (2020b)
Uranium flux from anoxic sediment (J_{anox})	6×10^{6} mol yr^{-1}	0	Zhang et al. (2020b)
K_{anox}	1.41×10^{-19}	0	Zhang et al. (2020b)
K_{oxic}	4.82×10^{-21}	0	Zhang et al. (2020b)

preferentially take up the heavier U isotopes (i.e., ^{238}U) from seawater, the predicted δ^{238}U value of ancient seawater, when the sources and sinks are balanced under a steady-state, will always be lower than (or equal to) that of the riverine input (Andersen et al., 2017; Lau et al., 2016). Therefore, we consider samples with δ^{238}U values higher than 0.1‰ (i.e., −0.26‰ + (0.26‰ ± 0.1‰)) to not record contemporaneous seawater δ^{238}U signal (Chen et al., 2018; Romaniello et al., 2013; Tissot and Dauphas, 2015). Here, the value of 0.26‰ ±0.1‰ represents an offset that is induced during early diagenetic processes and is applied to convert the carbonate δ^{238}U values to contemporaneous seawater δ^{238}U values according to Romaniello et al. (2013) and Chen et al. (2018).

In summary, our samples display no systematic correlation between the δ^{238}U excursions and indicators of detrital contamination (Al concentration, U/Al, and Rb/Sr ratios), meteoric diagenetic alteration (Mn/Sr ratios and Fe concentration), dolomitization (Sr concentration, Mg/Ca, and Sr/Ca ratios), and local pore water redox chemistry (U and Mo contents) that may produce a δ^{238}U offset from contemporaneous seawater (Fig. 4). Therefore, the δ^{238}U trends observed in the stratigraphic records can be reasonably interpreted as representative of secular changes in open marine δ^{238}U trends in the Permian seawater. Below, we explore the quantitative implications of our δ^{238}U record, although we acknowledge that additional studies from other coeval sections would strengthen our arguments.

5.2. Quantitative estimation of seafloor anoxia across the EPME and the EGE

We use a simple uranium isotope mass balance model to quantify the extent of seafloor anoxia across the PTB and the EGE following Lau et al. (2016) and Zhang et al. (2020b). Briefly, the model assumes U has a single major source (riverine inputs) to the oceans and two major sedimentary outputs (oxic and anoxic sinks) from the oceans (parameterization of the fluxes are detailed in Table 3). The dynamic uranium inventory in the seawater (N_{sw}) was computed using the methods described in Zhang et al. (2020b). The changing rate of N_{sw} and its isotopic composition can be described by ordinary differential equations by applying the law of mass balance (Lau et al., 2016; Zhang et al., 2020b):

$$\frac{dN_{SW}}{dt} = J_{riv} - J_{anox} - J_{oxic} \quad (1)$$

$$\frac{d(N_{SW} * \delta^{238}U_{sw})}{dt} = J_{riv} * \delta^{238}U_{riv} - J_{anox} * \delta^{238}U_{anox}$$

$$- J_{oxic} * \delta^{238}U_{oxic} \quad (2)$$

$$\delta^{238}U_{anox} = \delta^{238}U_{sw} + \Delta_{anox} \quad (3)$$

$$\delta^{238}U_{oxic} = \delta^{238}U_{sw} + \Delta_{oxic} \quad (4)$$

The fluxes of anoxic and oxic sink (J_{anox} and J_{oxic}) can be defined assuming a first-order dependence on the seawater U reservoir:

$$J_{anox} = K_{anox} * N_{SW} * A_{anox} \quad (5)$$

$$J_{oxic} = K_{oxic} * N_{SW} * A_{oxic} \quad (6)$$

The overall seafloor areas overlain by anoxic bottom waters (f_{anox}) can be expressed by:

$$f_{anox} = \frac{A_{anox}}{A_{ocean}} \quad (7)$$

where the subscript 'sw' is for seawater, 'riv' is for riverine input, 'anox' is for anoxic settings, and 'oxic' is for oxic settings. Δ_{anox} and Δ_{oxic} denote the isotopic differences between seawater and anoxic sinks and oxic sinks, respectively; A_{anox} and A_{ocean} denote seafloor areas overlain by anoxic waters and the entire seafloor areas of the ocean, respectively, where $A_{ocean} = A_{anox} + A_{oxic}$; f_{anox} corresponds to the fraction of total seafloor area overlain by anoxic waters at a given time, and K is the removal rate, which depends on the setting where U is removed.

Under the steady-state assumption, the resulting mass balance can be expressed as:

$$\delta^{238}U_{sw} = \delta^{238}U_{riv} - \frac{f_{anox} * K_{anox} * \Delta_{anox} + (1 - f_{anox}) * K_{oxic} * \Delta_{oxic}}{f_{anox} * K_{anox} + (1 - f_{anox}) * K_{oxic}} \quad (8)$$

and the extent of anoxia (the parts of the ocean with anoxic seafloor) can be obtained simply by solving for f_{anox} from Equation (8):

$$f_{anox} = \frac{\delta^{238}U_{riv} * K_{oxic} - \delta^{238}U_{oxic} * K_{oxic}}{\delta^{238}U_{riv} * (K_{oxic} - K_{anox}) - \delta^{238}U_{oxic} * K_{oxic} + \delta^{238}U_{anox} * K_{anox}} \quad (9)$$

The 95% confidence intervals for anoxic seafloor areas (f_{anox}) considering the analytical error of 0.07‰ and the uncertainty of the anoxic fractionation factor (Δ_{anox} from 0.68 to 0.99; Basu et al., 2014; Stirling et al., 2015; Stylo et al., 2015) were determined using a Monte Carlo approach with 10,000 realizations. In order to estimate the Permian seawater δ^{238}U values, a mean diagenetic offset of 0.26 ± 0.1‰ was subtracted from the marine carbonate δ^{238}U records because early diagenetic processes (i.e., before the carbonate muds become rocks) are known to induce a positive offset averaging 0.26 ± 0.1‰ compared to the overlying seawater (Chen et al., 2018; Romaniello et al., 2013; Tissot et al., 2018). Before making U-model calculations, we first interpolated and smoothed the measured δ^{238}U data using a LOWESS fit method with a span parameter value of 0.2 based on a cross-validation analysis. Considering that our study focuses on the pre-EPME intervals to provide background information leading to the EPME, and limited δ^{238}U data across the EPME were analyzed, we compiled the literature data across the EPME (note that there are no published δ^{238}U data across the EGE in the literature) to make a more compelling estimate of seafloor anoxia (Brennecka et al., 2011; Lau et al., 2016; Zhang et al., 2018a,b) (Fig. 5B).

The model results show that the f_{anox} stayed constant from the Kungurian (f_{anox} value of ~5%) to the Wordian stages and increased substantially from the early to the middle Capitanian, reaching a peak value during the EGE interval (f_{anox} value of ~10%) (Fig. 5B). During the middle to late Capitanian, the f_{anox} value decreased slowly and returned to the background level of the Permian in the early Wuchiapingian. The Wuchiapingian and most of the Changhsingian saw a steady ocean redox condition. The anoxic seafloor areas expanded sharply during the latest Changhsingian and f_{anox} reached a peak value of ~35% during the EPME (Fig. 5B, E). The estimated peak f_{anox} at the EGE ranges from 5% to 15% (95% confidence interval), while the peak f_{anox} at the EPME ranges from 29% to 39% (95% confidence interval), suggesting statistically significant difference between the sea floor anoxia event during the two biocrises. The anoxic seafloor areas during the EPME are three times larger (35% vs. 10%) than that during the EGE, while the duration of the anoxia during the EPME was significantly shorter (<0.1 Myr vs. >3 Myr) than that during the EGE (Fig. 5). These two episodes of marine anoxia expansion have also been independently documented by δ^{238}U records of low-magnesium calcite (LMC) in articulate brachiopod shells (Wang et al., 2022).

The two oceanic anoxic events coincided with the Emeishan LIP and the Siberian Traps LIP, respectively. The earliest intrusion associated with the Emeishan LIP was dated at 263 ± 3 Ma (Zhou et al., 2008), while the extrusive phase was dated to be 260.1 ± 1.2 Ma (Li et al., 2017). The termination age of the massive Emeishan flood basalts was 259.1 ± 0.5 Ma (Zhong et al., 2014) or 259.51 ± 0.21 Ma (Yang et al., 2018). The age model of the Siberian Traps LIP showed that the beginning of the pyroclastic eruption started before 252.24 ± 0.1 Ma (with a maximum age of about 255.58 ± 0.38 Ma) and two-thirds of the total erupted lava volume was emplaced between 252.24 ± 0.1 Ma (or 255.58 ± 0.38 Ma) and 251.907 ± 0.067 Ma (Burgess et al., 2017). Thus, the two episodes of expanded seafloor anoxic area during the EGE and the EPME can be temporally correlated with the ELIP and Siberian Traps LIP, respectively (Fig. 5). Volcanic CO_2 degassing can lead to the expansion of marine anoxia through (1) CO_2 – induced climatic warming, which can reduce oxygen solubility and result in sluggish oceanic circulation (Winguth et al., 2012), and (2) enhanced global chemical weathering, elevated nutrient levels in the oceans and higher primary marine productivity (Zhang et al., 2018b, 2020a). Below, we use a carbon cycle box model to explore the idea that the magnitudes in the extent of the expansion of marine anoxia and the ecosystem responses were closely related to the volcanic CO_2 emission rates.

5.3. Oceanic anoxia and ecosystem responses linked to volcanic carbon emission rates

Carbon cycle models serve as powerful tools to quantify CO_2 emissions during major carbon cycle perturbation intervals in geological history (Zeebe et al., 2009). The Long-term Ocean-Atmosphere-Sediment CArbon cycle Reservoir (LOSCAR) model has been widely used to constrain carbon emission patterns in the past, such as the Palaeocene-Eocene Thermal Maximum, the Cretaceous-Paleogene boundary, and the Triassic-Jurassic transition (Hull et al., 2020; Shen et al., 2022; Zeebe et al., 2009). LOSCAR is designed to calculate the partitioning of carbon between ocean, atmosphere, and sediments on various time scales and is suitable for simulating atmospheric pCO_2 and the surface ocean carbon isotopes during and after carbon injection over hundreds of thousands to millions of years. Owing to LOSCAR's high-efficiency numerical routine, thousands of different carbon perturbation scenarios with different parameter combinations (e.g., carbon sources, carbon emission amounts, and durations) can be tested with LOSCAR in parallel on the supercomputer within hours.

With LOSCAR, CO_2 emission rates and the most likely δ^{13}C values of the CO_2 sources across the EGE and the EPME are deter-

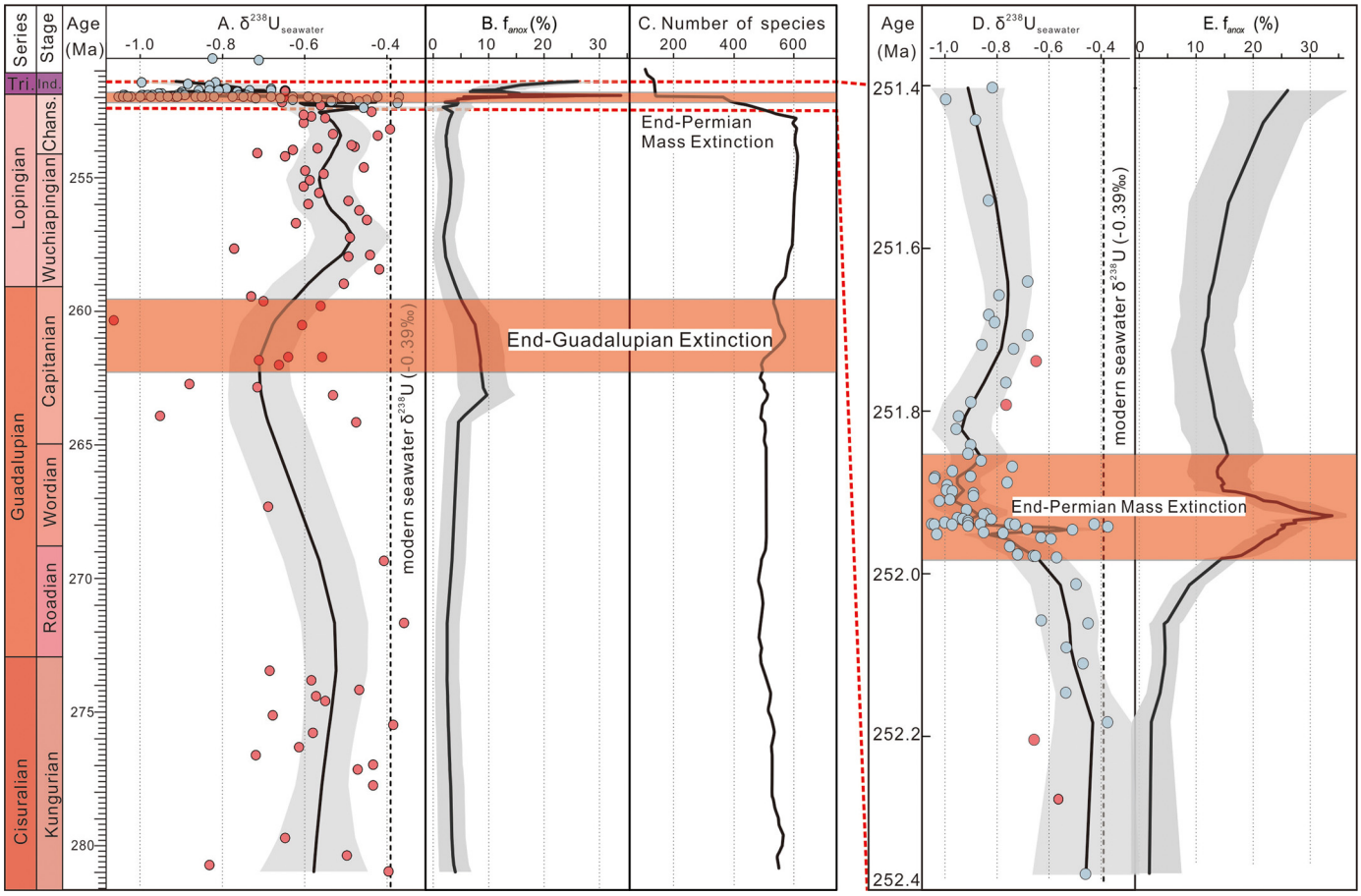

Fig. 5. A. $\delta^{238}U$ data of the seawater during the Permian, the blue circles represent previous data compiled from Zhang et al. (2018a, 2018b), Brennecka et al. (2011), and Lau et al. (2016) and the red circles represent this study; B. Calculated anoxic seafloor area based on uranium isotope mass balance model; C. The biodiversity changes during the Permian (Fan et al., 2020). D and F and the detailed information of the A and B across the Permian-Triassic boundary.

mined by minimizing the differences between modeled $\delta^{13}C_{carb}$, sea surface temperature, and surface ocean pH (when available). The $\delta^{13}C_{carb}$ data across the EPME and the EGE are from a global compilation of six sites in the Paleotethys Ocean, including Abadeh, Kuh-e-Ali Bashi, Shahreza and Zal sections in Iran (Korte et al., 2004; Richoz, 2006; Shen et al., 2013), and Dukou and Meishan sections in China (Shen et al., 2013; Fig. 6A,G). The simplified geologic settings and lithology of these sections are presented in the Supplementary Material. The sea surface temperature data of the EPME and the EGE are based on the conodont $\delta^{18}O$ data from sites in South China (Fig. 6; Appendix 2) and the pH data for the EPME are from brachiopod-based $\delta^{11}B$ measurements in Jurikova et al. (2020). According to the $\delta^{13}C$ record, the $\delta^{13}C$ excursion started at 252.02 Ma for the EPME and 261.5 Ma for the EGE, and lasted for ~120 kyr and ~2 Myr, respectively, until their initial recovery. To match the onset and duration of the $\delta^{13}C$ excursion to the volcanic eruption, the model runs started at 252.02 Ma for the EPME and 261.5 Ma for the EGE, and lasted for 120 kyr and 2 Myr, respectively (Fig. 6). To quantify the emission pattern and isotopic compositions of the carbon sources, we performed Monte Carlo resampling for emission trajectories and ran 5,000 LOSCAR models for both the EPME and the EGE. Specifically, we constructed 1,000 carbon emission trajectories (Fig. S2 and S7) for each assumed carbon emission source (reflected by different $\delta^{13}C$ values of −5‰, −8‰, −12‰, −18‰, and −25‰). To make our simulations more robust, we turned on the climate sensitivity parameter (i.e., the temperature change for a doubling of atmospheric CO_2) in LOSCAR and set its value to 3 (the unit of climate sensitivity is °C per doubling of CO_2 in ppmv). The LOSCAR simulation results (including average surface ocean $\delta^{13}C$ values, atmospheric pCO_2, average surface ocean temperature, and average surface ocean pH) are shown in Figures S3 to S6, and Figures S8 to S11 for the EPME and the EGE, respectively.

The modeled average surface ocean $\delta^{13}C$ output in each emission scenario was compared to the observed $\delta^{13}C_{carb}$ time series (by minimizing the mean squared error) to yield the best C emission trajectory for each assumed carbon isotope source for the EPME (Fig. S12A) and the EGE (Fig. S13A). The cumulative carbon emission amount, average surface ocean $\delta^{13}C$, atmospheric pCO_2, average surface ocean temperature, and average surface ocean pH (in relative scale) for each best emission scenario are also shown in Figure S12 and Figure S13. We then compare (visually) the surface ocean temperature and pH values of the five scenarios (i.e., of different carbon source isotope values) to the temperature and pH records (if any) to further constrain the best carbon sources.

For the EPME, the best-fit model scenario is associated with a $\delta^{13}C_{CO2}$ value between −8‰ to −12‰ (Fig. 6A-F), indicating a predominantly volcanic CO_2 source. This is in broad agreement with the Earth system modeling result pointing to a largely volcanic CO_2 source (Cui et al., 2021) but differs from the previous study suggesting the metamorphism of organic carbon (with $\delta^{13}C$ value of ~-25‰) is the main source of CO_2 (Svensen et al., 2009). When considering both the $\delta^{13}C$ excursion and the surface ocean pH decline simultaneously (Chen et al., 2016; Jurikova et al., 2020), rather than matching just the $\delta^{13}C$ excursion across the EPME (Svensen et al., 2009), we note that the $\delta^{13}C$ value (−25‰) associated with organic carbon oxidation is too low to generate the observed patterns of the $\delta^{13}C$ excursion, the surface

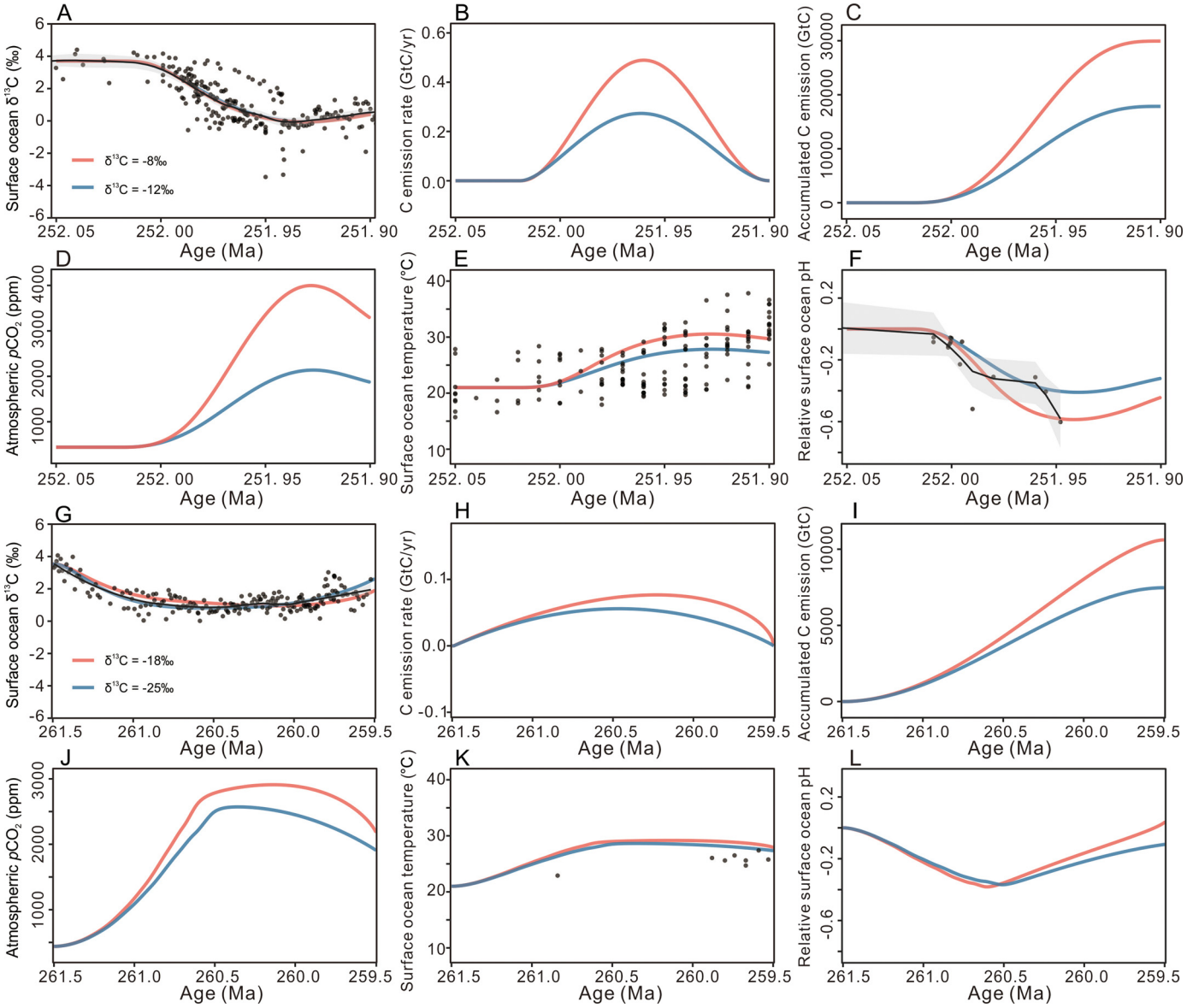

Fig. 6. The best LOSCAR model scenarios for the EPME (A-F) and the EGE (G-L). (A, G) Modeled average surface ocean $\delta^{13}C$ and observed $\delta^{13}C_{carb}$ data (black dots) compiled from the literature (Appendix 2); (B, H) Modeled carbon emission rate in Pg C yr^{-1}; (C, I) Modeled cumulative carbon emissions in Pg C (D, J) Modeled atmospheric CO_2 evolution (E, K) Modeled average surface ocean temperature and observed temperature (black dots) based on conodont proxy data (Appendix 2). (F, L) Modeled changes in average surface ocean pH compared with pH data (black dots in F) based on boron isotope proxy (Jurikova et al., 2020). The black line in F represents the loess-smoothed pH records with a span of 0.87 and the shaded gray area represents the 95% confidence interval of the smoothing fit.

ocean temperature, and pH records during the EPME. We also find that it is not necessary to invoke methane hydrate as a carbon source as suggested by Berner (2002) because the carbon isotope excursion of our study is smaller compared to those data used in the Berner (2002). Furthermore, our modeling results are in agreement with a modeling scenario proposed by Clarkson et al. (2015), such that a mixture of mantle and lighter carbon sources ($\delta^{13}C = -12.5‰$) could lead to the observed $\delta^{13}C$ pattern during the EPME. For the EGE, the carbon sources are difficult to be narrowed down due to the limited temperature records and the absence of pH records (Fig. 6G-L). However, existing coarse resolution temperature records across the EGE appear to support mainly ^{13}C-depleted carbon source (e.g., $\delta^{13}C = -18‰$ or $-25‰$, with $-25‰$ modeling result fitting slightly better with the temperature records; Fig. 6K), implying a mixture of volcanic and organic sources, with organic source as the dominating component. We highlight that the conclusion for the EGE was made based on the currently available records of $\delta^{238}U$, $\delta^{13}C$, and $\delta^{18}O$, and we suggest that higher-resolution proxy data for sea surface pH, surface ocean temperatures and redox conditions across the EGE will help further constrain the carbon sources and the emission trajectory. Comparing the carbon emission patterns between the EPME and the EGE (Fig. 6B and 6H), we argue that the peak emission rate of the EPME (~0.5 Pg C yr^{-1} for $-8‰$ and ~0.3 Pg C yr^{-1} for $-12‰$) is much faster (5 to 9 times) than that of the EGE (0.056 Pg C yr^{-1} for $-25‰$). The total amount of carbon emission from 252.02 Ma to 251.9 Ma during the EPME is estimated to range from 18,000 to 30,000 Pg C and the total amount of carbon emission from 261.5 Ma to 259.5 Ma during the EGE is estimated to be ~10,000 Pg C. The modeled peak pCO_2 is as high as ~4,000 ppm during the EPME and ~3,000 ppm during the EGE, consistent with CO_2 proxy data based on high-resolution $\delta^{13}C$ of C_3 plant (Wu et al., 2021). Both our modeled cumulative carbon emissions and degassing rates are within the range of the previous estimation for the EPME (Beerling et al., 2007; Cui et al., 2021; Sobolev et al., 2011).

A growing body of evidence suggests that the EGE was more protracted and taxonomic selective (Chen and Shen, 2021; Clapham et al., 2009; Fan et al., 2020) than the geologically instantaneous EPME (Burgess et al., 2014; Shen et al., 2019). Although the Emeishan and Siberian Traps LIPs have been overwhelmingly considered as the trigger of these events (Burgess et al., 2017; Shen et al., 2019), the driver for the drastically different ecosystem responses to the two LIPs events is less clear. The EGE was constrained between the conodont *Jinogondolella altudaensis* to *Clarkina postbitteri postbitteri* zones (Shen et al., 2020), generally coincident with the anoxic event recognized in our study. And the anoxic event during the end-Permian was coincided, or immediately preceded the EPME (Brennecka et al., 2011; Lau et al., 2016; Zhang et al., 2018a,b). By comparing the CO_2 emission rates, seafloor anoxic area changes, and changes in species richness, we suggest that the differences in the ecosystem responses across the EGE and the EPME can be reasonably attributed to the different emission rates of CO_2 associated with the ELIP and STLIP (Fig. 6). The comparison of CO_2 degassing between the two events suggests that the emission rate of CO_2 was more than five times faster during the EPME than the EGE (Fig. 6), similar to the timing of the onset of the expansion anoxic seafloor area (Fig. 5B). The anoxic seafloor area expanded sharply immediately prior to or coincident with the EPME, while the anoxic seafloor areas expanded slowly during the EGE. The differences in the rate and magnitude of volcanic CO_2 injection across EPME and EGE can reasonably account for the different extent in the expansion of marine anoxia. For example, a simple biogeochemical model suggests that the extent of marine anoxia depends strongly on the magnitudes of the CO_2 being injected into the ocean-atmosphere system (i.e., Fig. 7 in Zhang et al., 2020a). Similar expansion of anoxic seafloor area associated with CO_2 emissions has been documented during the end-Triassic (Jost et al., 2017), the end-Cretaceous (Clarkson et al., 2018), and the Paleocene-Eocene Thermal Maximum (Winguth et al., 2012). This led to the conclusion that the different extinction patterns during the EPME and the EGE are highly dependent on the carbon emission rate because of similar initial background climate conditions and ocean carbonate buffering capacity to CO_2 forcing (Fig. 5). One important aspect to point out is that there are large uncertainties on the total carbon emission amount and associated carbon isotope composition for the EGE due to the lack of constraints from high-resolution proxy records (such as surface ocean temperature and pH). We suggest that future studies with higher resolution and diverse proxy record are needed to validate our results.

6. Conclusions

We report a successive Middle (Guadalupian) to Late Permian (Lopingian) marine carbonate $\delta^{238}U$ data that reveal two episodes of widespread expansion of seafloor anoxia around the EGE and the EPME. The uranium mass balance model suggests that the anoxic seafloor areas were ~10% and ~35% during the EGE and the EPME, respectively. LOSCAR carbon cycle modeling suggests that the carbon emission rate across the EPME was at least five times faster than during the EGE, with the best-fit $\delta^{13}C$ values of the input sources being between −9 and −12‰ for the STLIP (indicating a predominant volcanic CO_2 source) and close to −25‰ for the ELIP (based on limited temperature records). More proxy data (e.g., seawater temperature, pH) are needed to better constrain the carbon source for the EGE. By linking the CO_2 emissions, changes in the marine redox chemistry, and the magnitude of marine extinctions, we find that the rate and the magnitude of the two Permian marine extinctions are closely linked to the CO_2 emission rates.

CRediT authorship contribution statement

Feifei Zhang and Shuzhong Shen conceived the study; Wenqian Wang, Quanfeng Zheng, Yichun Zhang, Dongxun Yuan, Shuzhong Shen joined fieldwork and contributed to sample collection; Wenqian Wang and Feifei Zhang, Shuang Zhang, Ying Cui, Hua Zhang did the isotopic analyses, data analyses, and model calculation; Wenqian Wang wrote the manuscript with contributions from all co-authors.

Declaration of competing interest

The authors declare that they have no known competing financial interests or personal relationships that could have appeared to influence the work reported in this paper.

Data availability

Data will be made available on request.

Acknowledgements

This research is supported by the Natural Science Foundation of China (42293280, 42073002, 91955201, 41830323, and 42103002), Strategic Priority Research Programs of the Chinese Academy of Sciences (XDB26000000), the Fundamental Research Funds for the Central Universities (0206-14380125), and Frontiers Science Center for Critical Earth Material Cycling Fund (DLTD2102). Y.C. was supported by NSF grant 2026877. S.Z. acknowledges support from the Data Science Career Initiation Fellow Program of Texas A&M Institute of Data Science. We appreciate the assistance of Xuefang Wu in helping with U isotope analysis at the Yale Metal Geochemistry Center. We also acknowledge Prof. Boswell Wing for editorial handling of this manuscript and two anonymous reviewers for constructive suggestions that improved the manuscript.

Appendix A. Supplementary material

Supplementary material related to this article can be found online at https://doi.org/10.1016/j.epsl.2022.117940.

References

Andersen, M.B., Stirling, C.H., Weyer, S., 2017. Uranium isotope fractionation. Rev. Mineral. Geochem. 82, 799–850.
Basu, A., Sanford, R.A., Johnson, T.M., Lundstrom, C.C., Löffler, F.E., 2014. Uranium isotopic fractionation factors during U(VI) reduction by bacterial isolates. Geochim. Cosmochim. Acta 136, 100–113.
Beerling, D.J., Harfoot, M., Lomax, B., Pyle, J.A., 2007. The stability of the stratospheric ozone layer during the end-Permian eruption of the Siberian Traps. Philos. Trans. A. Math. Phys. Eng. Sci. 365, 1843–1866.
Berner, R.A., 2002. Examination of hypotheses for the Permo-Triassic boundary extinction by carbon cycle modeling. Proc. Natl. Acad. Sci. USA 99, 4172–4177.
Bigeleisen, J., 1996. Nuclear size and shape effects in chemical reactions. Isotope chemistry of the heavy elements. J. Am. Chem. Soc. 118, 3676–3680.
Black, B.A., Neely, R.R., Lamarque, J.-F., Elkins-Tanton, L.T., Kiehl, J.T., Shields, C.A., Mills, M.J., Bardeen, C., 2018. Systemic swings in end-Permian climate from Siberian Traps carbon and sulfur outgassing. Nat. Geosci. 11, 949–954.
Bond, D.P.G., Wignall, P.B., Grasby, S.E., 2019. The Capitanian (Guadalupian, Middle Permian) mass extinction in NW Pangea (Borup Fiord, Arctic Canada): a global crisis driven by volcanism and anoxia. Geol. Soc. Am. Bull. 132, 931–942.
Brand, U., Veizer, J., 1980. Chemical diagenesis of a multicomponent carbonate system-1: trace elements. J. Sediment. Res. 50, 1219–1236.
Brennecka, G.A., Herrmann, A.D., Algeo, T.J., Anbar, A.D., 2011. Rapid expansion of oceanic anoxia immediately before the end-Permian mass extinction. Proc. Natl. Acad. Sci. 108, 17631–17634.
Burgess, S.D., Bowring, S.A., Shen, S.Z., 2014. High-precision timeline for Earth's most severe extinction. Proc. Natl. Acad. Sci. 111, 3316–3321.
Burgess, S.D., Muirhead, J.D., Bowring, S.A., 2017. Initial pulse of Siberian Traps sills as the trigger of the end-Permian mass extinction. Nat. Commun. 8, 164.

Chen, J., Shen, S.Z., 2021. Mid-Permian (End-Guadalupian) extinctions. In: Alderton, D., Elias, S.A. (Eds.), Encyclopedia of Geology, second edition. Academic Press, pp. 637–644.
Chen, J., Xu, Y.G., 2021. Permian large igneous provinces and their paleoenvironmental effects. In: Large Igneous Provinces, pp. 417–434.
Chen, J., Shen, S.Z., Li, X.H., Xu, Y.G., Joachimski, M.M., Bowring, S.A., Erwin, D.H., Yuan, D.X., Chen, B., Zhang, H., Wang, Y., Cao, C.Q., Zheng, Q.F., Mu, L., 2016. High-resolution SIMS oxygen isotope analysis on conodont apatite from South China and inplications for the end Permian mass extinction. Palaeogeogr. Palaeoclimatol. Palaeoecol. 448, 26–38.
Chen, X.M., Romaniello, S.J., Herrmann, A.D., Hardisty, D., Gill, B.C., Anbar, A.D., 2018. Diagenetic effects on uranium isotope fractionation in carbonate sediments from the Bahamas. Geochim. Cosmochim. Acta 237, 294–311.
Cheng, C., Li, S.Y., Xie, X.Y., Cao, T.L., Manger, W.L., Busbey, A.B., 2019. Permian carbon isotope and clay mineral records from the Xikou section, Zhen'an, Shaanxi Province, central China: climatological implications for the easternmost Paleo-Tethys. Palaeogeogr. Palaeoclimatol. Palaeoecol. 514, 407–422.
Clapham, M.E., Shen, S.Z., Bottjer, D.J., 2009. The double mass extinction revisited: reassessing the severity, selectivity, and causes of the end-Guadalupian biotic crisis (Late Permian). Paleobiology 35, 32–50.
Clarkson, M.O., Kasemann, S.A., Wood, R.A., Lenton, T.M., Daines, S.J., Richoz, S., Ohnemueller, F., Meixner, A., Poulton, S.W., Tipper, E.T., 2015. Ocean acidification and the Permo-Triassic mass extinction. Science 348, 229–232.
Clarkson, M.O., Stirling, C.H., Jenkyns, H.C., Dickson, A.J., Porcelli, D., Moy, C.M., Pogge von Strandmann, P.A.E., Cooke, I.R., Lenton, T.M., 2018. Uranium isotope evidence for two episodes of deoxygenation during Oceanic Anoxic Event 2. Proc. Natl. Acad. Sci. USA 115, 2918–2923.
Cui, Y., Li, M., van Soelen, E.E., Peterse, F., Kurschner, W.M., 2021. Massive and rapid predominantly volcanic CO_2 emission during the end-Permian mass extinction. Proc. Natl. Acad. Sci. USA 118, e2014701118.
Denison, R.E., Koepnick, R.B., Fletcher, A., Howell, M.W., Callaway, W.S., 1994. Criteria for the retention of original seawater $^{87}Sr/^{86}Sr$ in ancient shelf limestones. Chem. Geol. 112, 131–143.
Derry, L.A., Kaufman, A.J., Jacobsen, S.B., 1992. Sedimentary cycling and environmental change in the Late Proterozoic: evidence from stable and radiogenic isotopes. Geochim. Cosmochim. Acta 56, 1317–1329.
Ding, P.Z., Jin, T.A., Sun, X.F., 1989. Carboniferous-Permian boundary of Xikou area of Zhen'an, South Shaanxi, East Qinling Range. In: International Congress on Carboniferous Stratigraphy and Geology, Compte Rendu, Beijing, 1987, 11, pp. 199–206, 194.
Fan, J.X., Shen, S.Z., Erwin, D.H., Sadler, P.M., Macleod, N., Cheng, Q.M., Hou, X.D., Yang, J., Wang, X.D., Wang, Y., Zhang, H., Chen, X., Li, G.X., Zhang, Y.C., Shi, Y.K., Yuan, D.X., Chen, Q., Zhang, L.N., Li, C., Zhao, Y.Y., 2020. A high-resolution summary of Cambrian to Early Triassic marine invertebrate biodiversity. Science 367, 272–277.
Gilleaudeau, G.J., Romaniello, S.J., Luo, G., Kaufman, A.J., Zhang, F., Klaebe, R.M., Kah, L.C., Azmy, K., Bartley, J.K., Zheng, W., Knoll, A.H., Anbar, A.D., 2019. Uranium isotope evidence for limited euxinia in mid-Proterozoic oceans. Earth Planet. Sci. Lett. 521, 150–157.
Haq, B.U., Schutter, S.R., 2008. A chronology of Paleozoic sea-level changes. Science 322, 64–68.
Holmden, C., Amini, M., Francois, R., 2015. Uranium isotope fractionation in Saanich Inlet: a modern analog study of a paleoredox tracer. Geochim. Cosmochim. Acta 153, 202–215.
Hull, P.M., Bornemann, A., Penman, D., Henehan, M.J., Norris, R.D., Wilson, P.A., Blum, P., Alegret, L., Batenburg, S.J., Bown, P.R., Bralower, T.J., Cournede, C., Deutsch, A., Donner, B., Friedrich, O., Jehle, S., Kim, H., Kroon, D., Lippert, P.C., Loroch, D., Moebius, I., Moriya, K., Peppe, D.J., Ravizza, G.E., Röhl, U., Schueth, J.D., Sepúlveda, J., Sexton, P.F., Sibert, E.C., Śliwińska, K.K., Summons, R.E., Thomas, E., Westerhold, T., Whiteside, J.H., Yamaguchi, T., Zachos, J.C., 2020. On impact and volcanism across the Cretaceous-Paleogene boundary. Science 367, 266–272.
Jost, A.B., Bachan, A., van de Schootbrugge, B., Lau, K.V., Weaver, K.L., Maher, K., Payne, J.L., 2017. Uranium isotope evidence for an expansion of marine anoxia during the end-Triassic extinction. Geochem. Geophys. Geosyst. 18, 3093–3108.
Jurikova, H., Gutjahr, M., Wallmann, K., Flögel, S., Liebetrau, V., Posenato, R., Angiolini, L., Garbelli, C., Brand, U., Wiedenbeck, M., Eisenhauer, A., 2020. Permian–Triassic mass extinction pulses driven by major marine carbon cycle perturbations. Nat. Geosci. 13, 745–750.
Kaufman, A.J., Knoll, A.H., 1995. Neoproterozoic variations in the C-isotopic composition of seawater: stratigraphic and biogeochemical implications. Precambrian Res. 73, 27–49.
Korte, C., Kozur, H.W., Mohtat-Aghai, P., 2004. Dzhulfian to lowermost Triassic $\delta^{13}C$ record at the Permian/Triassic boundary section at Shahreza, Central Iran. Hallesches Jahrb. Geowiss. B, Beiheft 18, 73–78.
Korte, C., Jasper, T., Kozur, H.W., Veizer, J., 2006. $^{87}Sr/^{86}Sr$ record of Permian seawater. Palaeogeogr. Palaeoclimatol. Palaeoecol. 240, 89–107.
Lau, K.V., Maher, K., Altiner, D., Kelley, B.M., Kump, L.R., Lehrmann, D.J., Silva-Tamayo, J.C., Weaver, K.L., Yu, M., Payne, J.L., 2016. Marine anoxia and delayed Earth system recovery after the end-Permian extinction. Proc. Natl. Acad. Sci. USA 113, 2360–2365.
Li, Y.J., He, H.Y., Ivanov, A.V., Demonterova, E.I., Pan, Y.X., Deng, C.L., Zheng, D.W., Zhu, R.X., 2017. $^{40}Ar/^{39}Ar$ age of the onset of high-Ti phase of the Emeishan volcanism strengthens the link with the end-Guadalupian mass extinction. Int. Geol. Rev. 60, 1906–1917.
Richoz, S., 2006. Stratigraphie et variations isotopiques du carbone dans le Permien supérieur et le Trias inférieur de quelques localités de la Néotéthys (Turquie, Oman et Iran). Mém. Géol. Lausanne 46, 1–275.
Romaniello, S.J., Herrmann, A.D., Anbar, A.D., 2013. Uranium concentrations and $^{238}U/^{235}U$ isotope ratios in modern carbonates from the Bahamas: assessing a novel paleoredox proxy. Chem. Geol. 362, 305–316.
Rolison, J.M., Stirling, C.H., Middag, R., Rijkenberg, M.J.A., 2017. Uranium stable isotope fractionation in the Black Sea: modern calibration of the $^{238}U/^{235}U$ paleoredox proxy. Geochim. Cosmochim. Acta 203, 69–88.
Rudnick, R.L., Gao, S., 2014. Composition of the continental crust. In: Treatise on Geochemistry, pp. 1–51.
Scotese, C.R., 2021. An atlas of Phanerozoic paleogeographic maps: the seas come in and the seas go out. Annu. Rev. Earth Planet. Sci. 49 (1), 679–728.
Shen, J., Yin, R.S., Zhang, S., Algeo, T.J., Bottjer, D.J., Yu, J.X., Xu, G.Z., Penman, D., Wang, Y.D., Li, L.Q., Shi, X., Planavsky, N.J., Feng, Q.L., Xie, S.C., 2022. Intensified continental chemical weathering and carbon-cycle perturbations linked to volcanism during the Triassic-Jurassic transition. Nat. Commun. 13, 299.
Shen, S.Z., Cao, C.Q., Zhang, H., Bowring, S.A., Henderson, C.M., Payne, J.L., Davydov, V.I., Chen, B., Yuan, D.X., Zhang, Y.C., Wang, W., Zheng, Q.F., 2013. High-resolution $\delta^{13}C_{carb}$ chemostratigraphy from latest Guadalupian through earliest Triassic in South China and Iran. Earth Planet. Sci. Lett. 375, 156–165.
Shen, S.Z., Zhang, H., Zhang, Y.C., Yuan, D.X., Chen, B., He, W.H., Mu, L., Lin, W., Wang, W.Q., Chen, J., Wu, Q., Cao, C.Q., Wang, Y., Wang, X.D., 2019. Permian integrative stratigraphy and timescale of China. Sci. China Earth Sci. 62, 154–188.
Shen, S.Z., Yuan, D.X., Henderson, C.M., Wu, Q., Zhang, Y.C., Zhang, H., Mu, L., Ramezani, J., Wang, X.D., Lambert, L.L., Erwin, D.H., Hearst, J.M., Xiang, L., Chen, B., Fan, J.X., Wang, Y., Wang, W.Q., Qi, Y.P., Chen, J., Qie, W.K., Wang, T.T., 2020. Progress, problems and prospects: an overview of the Guadalupian Series of South China and North America. Earth-Sci. Rev. 211.
Shi, Y.K., Wang, X.D., Fan, J.X., Huang, H., Xu, H.Q., Zhao, Y.Y., Shen, S.Z., 2021. Carboniferous-earliest Permian marine biodiversification event (CPBE) during the Late Paleozoic Ice Age. Earth-Sci. Rev. 220, 103699.
Sobolev, S.V., Sobolev, A.V., Kuzmin, D.V., Krivolutskaya, N.A., Petrunin, A.G., Arndt, N.T., Radko, V.A., Vasiliev, Y.R., 2011. Linking mantle plumes, large igneous provinces and environmental catastrophes. Nature 477, 312–316.
Stirling, C.H., Andersen, M.B., Warthmann, R., Halliday, A.N., 2015. Isotope fractionation of ^{238}U and ^{235}U during biologically-mediated uranium reduction. Geochim. Cosmochim. Acta 163, 200–218.
Stylo, M., Neubert, N., Wang, Y., Monga, N., Romaniello, S.J., Weyer, S., Bernier- Latmani, R., 2015. Uranium isotopes fingerprint biotic reduction. Proc. Natl. Acad. Sci. USA 112 (18), 5619–5624.
Svensen, H., Planke, S., Polozov, A.G., Schmidbauer, N., Corfu, F., Podladchikov, Y.Y., Jamtveit, B., 2009. Siberian gas venting and the end-Permian environmental crisis. Earth Planet. Sci. Lett. 277, 490–500.
Tissot, F.L.H., Dauphas, N., 2015. Uranium isotopic compositions of the crust and ocean: age corrections, U budget and global extent of modern anoxia. Geochim. Cosmochim. Acta 167, 113–143.
Tissot, F.L.H., Chen, C., Go, B.M., Naziemiec, M., Healy, G., Bekker, A., Swart, P.K., Dauphas, N., 2018. Controls of eustasy and diagenesis on the $^{238}U/^{235}U$ of carbonates and evolution of the seawater ($^{234}U/^{238}U$) during the last 1.4 Myr. Geochim. Cosmochim. Acta 242, 233–265.
Tostevin, R., Clarkson, M.O., Gangl, S., Shields, G.A., Wood, R.A., Bowyer, F., Penny, A.M., Stirling, C.H., 2019. Uranium isotope evidence for an expansion of anoxia in terminal Ediacaran oceans. Earth Planet. Sci. Lett. 506, 104–112.
Viglietti, P.A., Benson, R.B.J., Smith, R.M.H., Botha, J., Kammerer, C.F., Skosan, Z., Butler, E., Crean, A., Eloff, B., Kaal, S., Mohoi, J., Molehe, W., Mtalana, N., Mtungata, S., Ntheri, N., Ntsala, T., Nyaphuli, J., October, P., Skinner, G., Strong, M., Stummer, H., Wolvaardt, F.P., Angielczyk, K.D., 2021. Evidence from South Africa for a protracted end-Permian extinction on land. Proc. Natl. Acad. Sci. USA 118.
Wang, W.Q., Katchinoff, J.A.R., Garbelli, C., Immenhauser, A., Zheng, Q.F., Zhang, Y.C., Yuan, D.X., Shi, Y.K., Wang, J.Y., Planavsky, N., Shen, S.Z., 2021. Revisiting the Permian seawater $^{87}Sr/^{86}Sr$ record: new perspectives from brachiopod proxy data and stochastic oceanic box models. Earth-Sci. Rev. 218, 103679.
Wang, W.Q., Zhang, F.F., Shen, S.Z., Bizzarro, M., Garbelli, C., Zheng, Q.F., Zhang, Y.C., Yuan, D.X., Shi, Y.K., Cao, M., Dahl, T.W., 2022. Constraining marine anoxia under the extremely oxygenated Permian atmosphere using uranium isotopes in calcitic brachiopods and marine carbonates. Earth Planet. Sci. Lett. 594, 117714.
White, D.A., Elrick, M., Romaniello, S., Zhang, F., 2018. Global seawater redox trends during the Late Devonian mass extinction detected using U isotopes of marine limestones. Earth Planet. Sci. Lett. 503, 68–77.
Winguth, A.M.E., Thomas, E., Winguth, C., 2012. Global decline in ocean ventilation, oxygenation, and productivity during the Paleocene-Eocene Thermal Maximum: implications for the benthic extinction. Geology 40, 263–266.
Wu, Q., Ramezani, J., Zhang, H., Yuan, D.X., Erwin, D.H., Henderson, C.M., Lambert, L.L., Zhang, Y.C., Shen, S.Z., 2020. High-precision U-Pb zircon age constraints on the Guadalupian in West Texas, USA. Palaeogeogr. Palaeoclimatol. Palaeoecol. 548, 109668.

Wu, Y.Y., Chu, D.L., Tong, J.N., Song, H.J., Dal Corso, J., Wignall, P.B., Song, H.Y., Du, Y., Cui, Y., 2021. Six-fold increase of atmospheric pCO_2 during the Permian-Triassic mass extinction. Nat. Commun. 12, 2137.

Yan, D.T., Zhang, L.Q., Qiu, Z., 2013. Carbon and sulfur isotopic fluctuations associated with the end-Guadalupian mass extinction in South China. Gondwana Res. 24, 1276–1282.

Yang, J.H., Cawood, P.A., Du, Y.S., Condon, D.J., Yan, J.X., Liu, J.Z., Huang, Y., Yuan, D.X., 2018. Early Wuchiapingian cooling linked to Emeishan basaltic weathering? Earth Planet. Sci. Lett. 492, 102–111.

Zeebe, R.E., Zachos, J.C., Dickens, G.R., 2009. Carbon dioxide forcing alone insufficient to explain Palaeocene-Eocene Thermal Maximum warming. Nat. Geosci. 2, 576–580.

Zhang, F.F., Algeo, T.J., Romaniello, S.J., Cui, Y., Zhao, L.S., Chen, Z.Q., Anbar, A.D., 2018a. Congruent Permian-Triassic $\delta^{238}U$ records at Panthalassic and Tethyan sites: confirmation of global-oceanic anoxia and validation of the U-isotope paleoredox proxy. Geology 46, 327–330.

Zhang, F.F., Romaniello, S.J., Algeo, T.J., Lau, K.V., Clapham, M.E., Richoz, S., Herrmann, A.D., Smith, H., Horacek, M., Anbar, A.D., 2018b. Multiple episodes of extensive marine anoxia linked to global warming and continental weathering following the latest Permian mass extinction. Sci. Adv. 4, e1602921.

Zhang, F.F., Xiao, S.H., Kendall, B., Romaniello, S.J., Cui, H., Meyer, M., Gilleaudeau, G.J., Kaufman, A.J., Anbar, A.D., 2018c. Extensive marine anoxia during the terminal Ediacaran period. Sci. Adv. 4 (6), eaan8983.

Zhang, F.F., Dahl, T.W., Lenton, T.M., Luo, G., Shen, S.Z., Algeo, T.J., Planavsky, N., Liu, J.S., Cui, Y., Qie, W.K., Romaniello, S.J., Anbar, A.D., 2020a. Extensive marine anoxia associated with the Late Devonian Hangenberg Crisis. Earth Planet. Sci. Lett. 533, 115976.

Zhang, F.F., Lenton, T.M., del Rey, Á., Romaniello, S.J., Chen, X.M., Planavsky, N.J., Clarkson, M.O., Dahl, T.W., Lau, K.V., Wang, W.Q., Li, Z.H., Zhao, M., Isson, T., Algeo, T.J., Anbar, A.D., 2020b. Uranium isotopes in marine carbonates as a global ocean paleoredox proxy: a critical review. Geochim. Cosmochim. Acta 287, 27–49.

Zhang, H., Zhang, F.F., Chen, J.B., Erwin, D.H., Syverson, D.D., Ni, P., Rampino, M., Chi, Z., Cai, Y.F., Xiang, L., Li, W.Q., Liu, S.A., Wang, R.C., Wang, X.D., Feng, Z., Li, H.M., Zhang, T., Cai, H.M., Zheng, W., Cui, Y., Zhu, X.K., Hou, Z.Q., Wu, F.Y., Xu, Y.G., Planavsky, N., Shen, S.Z., 2021. Felsic volcanism as a factor driving the end-Permian mass extinction. Sci. Adv. 7, eabh1390.

Zhong, Y.T., He, B., Mundil, R., Xu, Y.G., 2014. CA-TIMS zircon U–Pb dating of felsic ignimbrite from the Binchuan section: implications for the termination age of Emeishan large igneous province. Lithos 204, 14–19.

Zhou, M.F., Arndt, N.T., Malpas, J., Wang, C.Y., Kennedy, A.K., 2008. Two magma series and associated ore deposit types in the Permian Emeishan large igneous province, SW China. Lithos 103, 352–368.